PHYSICAL REVIEW B **86**, 104106 (2012)

Size estimation of embedded Cu nanoprecipitates in Fe by using affinitively trapped positrons

T. Toyama,[1] Z. Tang,[2,3] K. Inoue,[1,4] T. Chiba,[1] T. Ohkubo,[5] K. Hono,[5] Y. Nagai,[1] and M. Hasegawa[2,6]

[1]*International Research Center for Nuclear Materials Science, Institute for Materials Research, Tohoku University, Oarai, Ibaraki 311-1313, Japan*

[2]*Institute for Materials Research, Tohoku University, Sendai, Miyagi 980-8577, Japan*

[3]*Key Laboratory of Polar Materials and Devices (Ministry of Education of China), East China Normal University, Shanghai 200241, People's Republic of China*

[4]*Department of Materials Science and Engineering, Graduate School of Engineering, Kyoto University, Kyoto, Kyoto 606-8501, Japan*

[5]*National Institute for Materials Science, Tsukuba, Ibaraki 305-0047, Japan*

[6]*Cyclotron and Radioisotope Center, Tohoku University, Sendai, Miyagi 980-8578, Japan*

(Received 31 August 2011; revised manuscript received 14 March 2012; published 13 September 2012)

By utilizing a unique characteristic of the affinitively trapped positrons, here we demonstrate a powerful method to estimate the sizes of the embedded Cu nanoprecipitates (and subnanoprecipitates) (ECNPs) in Fe. The positron-electron momentum density distributions in the ECNPs with various sizes in a thermally aged Fe-Cu dilute alloy were measured by using the two-dimensional angular correlation of positron annihilation radiation technique and the momentum smearing around the Fermi cutoff was clearly observed. It is clarified that this smearing effect is proportional to the inverse of the average radii of the ECNPs and thus it can be employed to estimate the ECNPs' sizes. Moreover, the ECNPs' sizes obtained by the present method are compared with those obtained by the three-dimensional atom probe technique and good agreement is observed, justifying the size estimation using the smearing effect. It is noteworthy that the present technique can detect the smearing due to the ECNPs with their radii even below about 0.5 nm and thus gives an important trend in the smearing reflecting the average size of the ECNPs in this range.

DOI: 10.1103/PhysRevB.86.104106 PACS number(s): 78.70.Bj, 81.20.Fw, 61.46.Df, 71.18.+y

I. INTRODUCTION

Embedded nanoparticles (and subnanoparticles) (ENPs) in materials, such as ultrafine precipitates and quantum dots in electronic and structural materials, play an important role for a variety of prospective industrial applications. Therefore, characterization of the ENPs, such as size, number density, chemical composition, and electronic structure, is essential for understanding their physical and mechanical properties. We have been developing various methods for characterization of ENPs using positron annihilation techniques. For example, recently we have successfully developed an efficient method to obtain a number density of ENPs using positron annihilation age-momentum correlation.[1] In this work we propose a method to estimate the size of ENPs using smearing effects in the momentum distribution of positron-electron ($e^+ - e^-$) pairs annihilating in the ENPs.

Positron annihilation technique has been known as a powerful tool to study vacancies and their aggregations in solids because positrons can be sensitively trapped at vacancy-type defects. Furthermore, it had been expected that positrons could also be confined in ENPs and precipitates with positron affinities higher than that of the host material, even if the sites are free from vacancy-type defects.[2,3] For example, positron affinitive trapping to embedded Cu nanoprecipitates (ECNPs) in Fe matrix, which play a significant role in the embrittlement of nuclear reactor pressure vessel steels,[4] had been suggested based on the calculation of positron affinities and positron lifetime measurement.[5,6] Recently, by using coincidence Doppler broadening of positron annihilation, the positron confinement to the ECNPs' matrix by the affinitive trapping has been evidenced.[7–9] The confined positrons annihilate with the electrons of the ENPs and thus bring site-selective information on the microscopic and electronic structures of the ENPs through two emitted annihilation γ photons. By measuring the angular correlation distribution between the two γ photons, i.e., angular correlation of positron annihilation radiation (ACAR), the $e^+ - e^-$ momentum density distributions in ENPs are directly obtained experimentally. For example, the Fermi surface of ECNPs in an Fe matrix[8] and of embedded Ag, Zn,[9] and Li nanoparticles[10] in an Al matrix have been obtained by using two-dimensional (2D) ACAR.

Positron confinement in a quantum dot and the consequent exclusive sampling effect to the electronic structures of the quantum dot lead to a smearing of $e^+ - e^-$ the momentum density distribution around the Fermi momentum p_F, as reported in CdSe quantum dots[11] and nanovoids in Al.[12] For the ECNPs in Fe single-crystal samples, we have directly observed such a smearing phenomenon in momentum space: Figure 1 shows contour plots of the three-dimensional reconstruction of the $e^+ - e^-$ momentum density distribution of bcc ECNPs (top) and fcc bulk Cu (bottom).[13] In the ECNPs, the cutoff around p_F (~0.71 a.u.) is blurred compared to that of bulk Cu, which is evidence of the smearing effect in the momentum distribution in the ECNPs. By a first-principles calculation of the ECNPs in Fe, we have recently predicted that, due to the sampling effect of the trapped positrons in the nanoclusters of Cu_6–Cu_{59}, there is a size-dependent smearing that scales linearly with $\Omega^{-1/3}$, where Ω is the ECNPs' volume.[14] Therefore, it is expected that the smearing phenomenon gives us information on the sizes of ENPs in the bulk matrix, as we have preliminarily reported.[15] Then as a representative case, we apply this method to the ECNPs in the Fe matrix.

In this paper we demonstrate that the size of ECNPs in Fe-Cu alloys can be estimated by using the unique characteristic of the positron affinitive confinement in the ECNPs. For

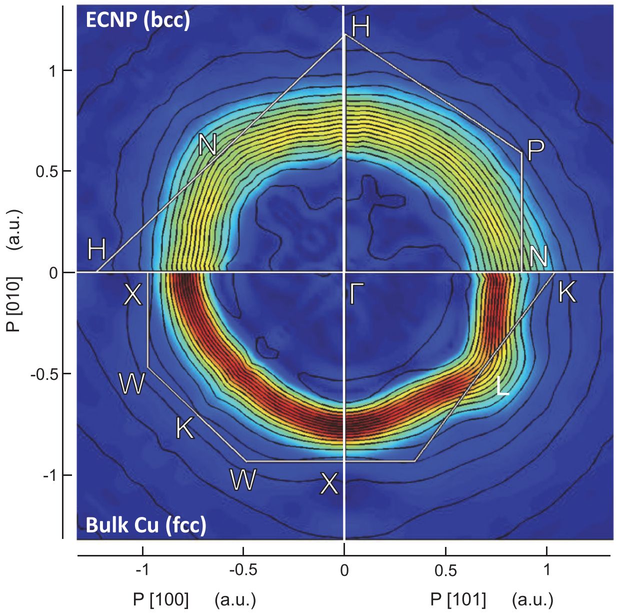

FIG. 1. (Color online) Contour plots of the 3D reconstruction of the e^+-e^- momentum density distribution of bcc ECNPs (top) and fcc bulk Cu (bottom). Contour spacing is 6.6% of the peak height. The bcc and fcc Brillouin zone boundaries and symmetry points are indicated.

various sizes of ECNPs formed by thermal aging, the $e^+ - e^-$ momentum density distribution in the ECNPs was measured by using the 2D-ACAR technique. This technique enables the direct quantification of the smearing due to the superb momentum resolution compared with the Doppler broadening method used in previous reports.[11] We will show by a 2D-ACAR experiment that the smearing effect scales linearly with the inverse of the average radius of ECNPs. Based on this, the average radius of ECNPs is estimated and compared with those obtained by using a 3D atom probe (AP). The results agree with each other, justifying the size estimation based on the smearing effect.

II. EXPERIMENT

A. Methods

The 2D-ACAR technique measures the 2D projection of the $e^+ - e^-$ momentum density distribution, which reflects the Fermi surface topology directly. The details of this method are described in Refs. 16–18. Two-dimensional ACAR spectra of the Fe-Cu samples, as well as two reference samples (well-annealed pure Cu and pure Fe), were obtained using an Anger-camera-type 2D-ACAR apparatus. About 5×10^7 annihilation events were accumulated for each 2D-ACAR spectrum and the overall momentum resolution was 0.11 a.u. Because polycrystalline Fe-Cu samples were used in the present study, the experimental 2D-ACAR spectra were averaged over crystal orientation and isotropic. Thus hereafter we focus on the radial momentum distributions, i.e., the cylindrical average of the 2D-ACAR spectra.

It should be noted that the accumulated annihilation events come from not only the trapped positrons annihilated in the ECNPs but also the positrons annihilated in the Fe matrix. To subtract the latter contribution, we have to estimate its fraction in the total 2D-ACAR spectrum. This is achieved by measuring the coincidence Doppler broadening (CDB) spectra. The CDB technique profiles the 1D projection of the $e^+ - e^-$ momentum density distribution along the emission direction of the annihilation γ photons.[19] The CDB technique can measure the momentum distribution of elementally specific inner orbital electrons and thus enables chemical identification of the positron annihilation sites. About 2×10^7 annihilation events were accumulated for each CDB measurement.

B. Sample preparation

The Fe-Cu (1.0 wt.% Cu) polycrystal samples were prepared from high-purity Fe (4*N*) and Cu (5*N*) by arc melting. Disks 5 mm in diameter and 0.3 mm thick and 10×10 mm^2 sheets 0.5 mm thick were prepared and annealed at 825 °C for 4 h, followed by quenching into iced water. The sheets were cut into $(10 \times 0.5 \times 0.5)$-mm^3 rods. The disks and rods were for positron annihilation and 3D-AP measurements, respectively. The samples were aged at 475 °C for 0.1–20 h to form the ECNPs with various sizes.

The sizes of ECNPs were obtained by using the well-established 3D-AP technique.[20,21] Three-dimensional AP measurements were carried out with a Tomographic Atom Probe by CAMECA, under conditions of a voltage pulse fraction of 20%, a dc voltage in a range from 5 to 10 kV, and a specimen temperature of 50 K. Three-dimensional AP atom maps of Cu in the aged Fe-Cu samples are shown in Fig. 2. The Cu atoms were in a supersaturated solid solution in the as-quenched sample. Aggregations of Cu atoms were observed after 0.5 and 1 h of aging as indicated by arrows, but no such aggregations could be observed in the 3D-AP atom maps after short-time thermal aging, i.e., 0.1–0.3 h. Embedded Cu nanoprecipitates were clearly observed after 2 h of aging and coarsened after 10 and 20 h of aging. The thermal aging evolution of the average radius of ECNPs obtained by a 3D-AP is listed in Table I. In the evaluation of the average radius, we assume that the ECNPs are pure Cu.[1,7,8]

III. RESULTS

Figure 3 shows the ratio curves of the CDB spectra normalized to bcc Fe for the aged Fe-Cu and for fcc pure Cu as a reference. For the as-quenched Fe-Cu, the ratio curve is almost on the horizontal line at 1.0. This means that the positrons are not trapped by the isolated Cu atoms in the supersaturated solid solution but annihilate only with the electrons of Fe atoms. As thermal aging proceeds, pronounced peaks are found at the high momentum region around 3.3 a.u. These peaks are ascribed to the characteristic momentum distribution of the closed 3*d* shell of Cu, as shown by our previous works,[7,22] indicating positron trapping at the ECNPs. It is noteworthy that even in the very early stage, i.e., after 0.1–0.3 h of aging, the positron can detect ECNPs with a high sensitivity, whereas the 3D-AP observed almost no ECNPs, as shown in Fig. 2. We can estimate the fractions of the positron annihilation at the ECNPs from the relative intensity of the observed pronounced peaks with respect to the peak intensity of pure Cu.[23,24] The obtained fractions of the positron annihilation in the ECNPs are listed in Table II. The fraction increases with the aging time.

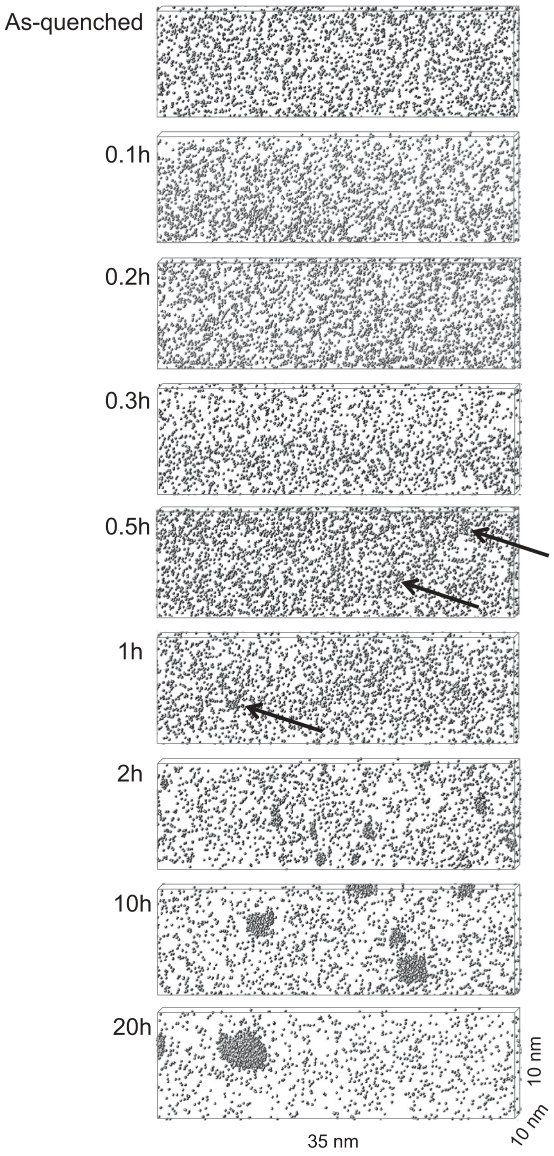

FIG. 2. Three-dimensional AP atom maps of Cu in thermal-aged Fe-Cu. The ECNPs after 0.5 and 1 h of aging are indicated by arrows.

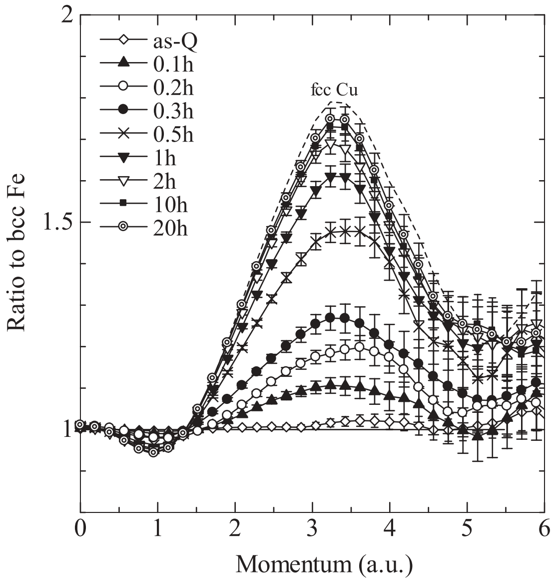

FIG. 3. Ratio curves of the CDB spectra of the aged Fe-Cu and fcc Cu as a reference. All the CDB spectra are normalized to bcc Fe.

The cylindrical averages of 2D-ACAR spectra, N_{ACAR}, of the aged Fe-Cu, and of fcc Cu and bcc Fe as references are shown in Fig. 4(a). The N_{ACAR} after 0.2 h of aging is almost identical to that of bcc Fe. As thermal aging proceeds, N_{ACAR} of Fe-Cu becomes close to that of fcc Cu. By using the fractions listed in Table II, we subtract the component of positron annihilation in the Fe matrix from the observed N_{ACAR} of the Fe-Cu to obtain the components of positron annihilation in the ECNPs, $N_{\mathrm{ACAR}}^{\mathrm{ECNP}}$. The $N_{\mathrm{ACAR}}^{\mathrm{ECNP}}$ are shown in Fig. 4(b) The N_{ACAR} of fcc Cu are also shown as a reference. The $N_{\mathrm{ACAR}}^{\mathrm{ECNP}}$ after 0.2 h of aging is higher than N_{ACAR} of fcc Cu in the momentum region higher than the Fermi momentum ($p > p_F$) while lower than N_{ACAR} of fcc Cu in the lower momentum region ($p < p_F$). This clearly evidences the smearing effect of the $e^+ - e^-$ momentum density distribution in ECNPs. The $N_{\mathrm{ACAR}}^{\mathrm{ECNP}}$ becomes close to the N_{ACAR} of fcc Cu with aging time. This shows that the smearing effect becomes less significant with aging time. We list the variation of the average size of ECNPs estimated by the 3D-AP with aging time in Table I, which shows clearly that the aging-time evolution of $N_{\mathrm{ACAR}}^{\mathrm{ECNP}}$ reflects the size dependence of the smearing effect.

To explore the smearing effect more explicitly, we extract the difference between $N_{\mathrm{ACAR}}^{\mathrm{ECNP}}$ of the aged Fe-Cu and N_{ACAR} of *bulk* bcc Cu. Here we note that the $N_{\mathrm{ACAR}}^{\mathrm{ECNP}}$ after 20 h of aging is very close to that of pure (fcc) Cu. This indicates that the smearing effect after 20 h is negligibly small. Therefore,

TABLE I. Thermal aging evolution of the average radius of the ECNPs obtained by 3D-AP.

Aging time (h)	Average radius of the ENCPs (nm)
0.1	
0.2	
0.3	
0.5	0.39
1	0.42
2	0.65
10	1.0
20	1.6

TABLE II. Thermal aging evolution of the fractions of positron annihilation in the ECNPs.

Aging time (h)	Fraction of positron annihilation in the ECNPs (%)
0	~0
0.1	13
0.2	24
0.3	35
0.5	61
1	76
2	87
10	92
20	95

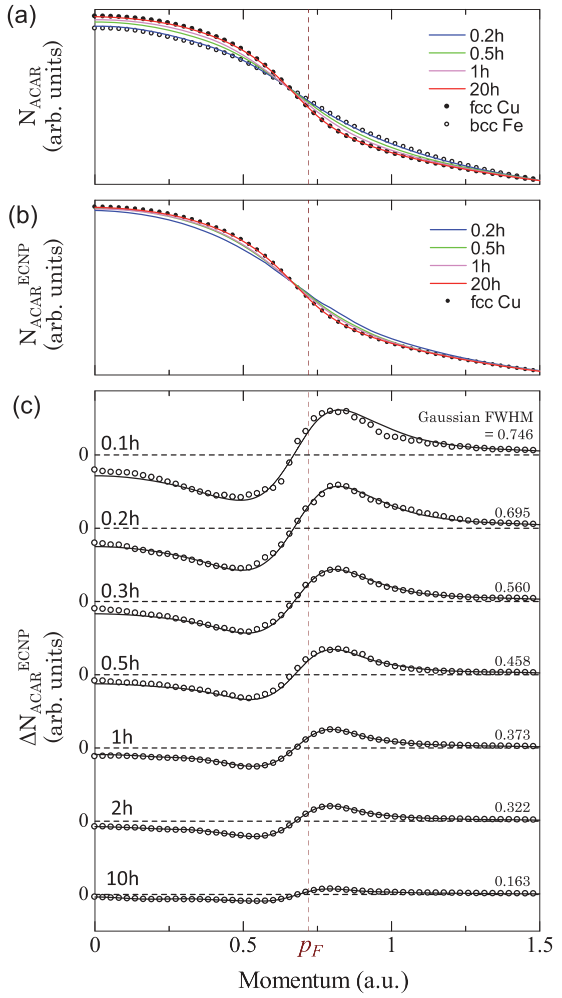

FIG. 4. (Color) (a) Cylindrical averages of 2D-ACAR spectra (N_{ACAR}) of the aged Fe-Cu and of fcc Cu and bcc Fe as references, (b) the N_{ACAR} components at the ECNPs ($N_{\mathrm{ACAR}}^{\mathrm{ECNP}}$) and N_{ACAR} of fcc Cu as a reference, and (c) the differences between $N_{\mathrm{ACAR}}^{\mathrm{ECNP}}$ for 0.1–10 h of aging and that of 20 h of aging ($\Delta N_{\mathrm{ACAR}}^{\mathrm{ECNP}}$, open circles). The solid lines show the best fittings with the Gaussian function convolution to $N_{\mathrm{ACAR}}^{\mathrm{ECNP}}$ for 20 h of aging for each $\Delta N_{\mathrm{ACAR}}^{\mathrm{ECNP}}$ for 0.1–10 h of aging. The FWHM of the fitting Gaussian functions are shown in a.u. The Fermi momentum ($p_F \sim 0.71$ a.u.) is also given.

we employed the $N_{\mathrm{ACAR}}^{\mathrm{ECNP}}$ after 20 h of aging as a good approximation to N_{ACAR} of the bulk bcc Cu. The open circles in Fig. 4(c) show $\Delta N_{\mathrm{ACAR}}^{\mathrm{ECNP}}$, which are the differences of $N_{\mathrm{ACAR}}^{\mathrm{ECNP}}$ after 0.1–10 h of aging from that of 20 h of aging. The $\Delta N_{\mathrm{ACAR}}^{\mathrm{ECNP}}$ is mostly negative in momentum region lower than p_F and positive in momentum region higher than p_F. This characteristic feature decreases with increasing aging time, demonstrating explicitly the aging-time evolution of the smearing effect. The smearing effect is then assessed quantitatively; the solid lines in Fig. 4(c) show the best fittings with the Gaussian function convolution to $N_{\mathrm{ACAR}}^{\mathrm{ECNP}}$ of 20-h-aged Fe-Cu for each $\Delta N_{\mathrm{ACAR}}^{\mathrm{ECNP}}$ after 0.1–10 h of aging. It is observed that the $\Delta N_{\mathrm{ACAR}}^{\mathrm{ECNP}}$ curves are well reproduced by the solid lines. Therefore we take the full width of the half maximum (FWHM) of the fitting Gaussian functions as the measures of the smearing effect Δp, as listed in Fig. 4(c).

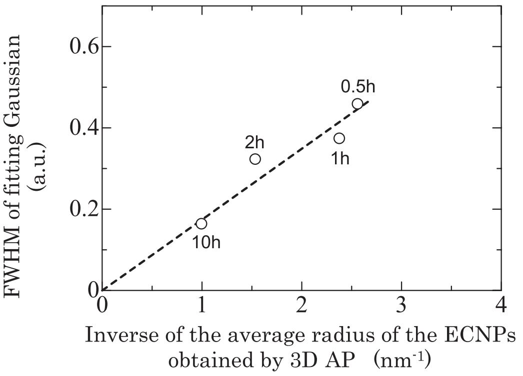

FIG. 5. Correlation of the FWHM of the fitting Gaussian functions and the inverse of the average radius of ECNPs listed in Table I.

The average radii of the ECNPs were also measured by using the 3D-AP after aging longer than 0.5 h (Table I) and the correlation between Δp and the inverse of the average radius of ECNPs (r^{-1}) is shown in Fig. 5 together with the dashed line as a guide to the eye. The linear relationship between Δp and r^{-1}, i.e., $\Delta p \propto r^{-1}$, is clearly demonstrated.

IV. DISCUSSION

As shown in Fig. 5, the linear relationship between the FWHM of the fitting Gaussian reflecting smearing effect and the inverse of the average radius of ECNPs is clearly seen. A similar momentum smearing effect with an r^{-2} size dependence (where r is the radius of the quantum dots) has been observed experimentally in the CdSe quantum dots.[11] Saniz *et al.*[25] discussed theoretically both the confinements of the electrons and positrons and their contributions to the smearing effect based on a model of positron annihilation in a confined electron gas. They showed that the observed smearing effect mainly originates from the quantum size effect of the electron confinement with an r^{-1} size dependence, while the positron's confinement leads to a small correction to the smearing.

However, the electron confinement cannot be the origin of the present case because no electron confinement potential is expected between bcc Cu and bcc Fe, which are gapless metals with similar valence bandwidths. Here we propose a more general origin of the smearing effect as the result of a break of the long-range phase coherence of the atomic (Wannier) orbitals due to the heterostructure and the sampling effect of the trapped positrons in ECNPs. To demonstrate this origin, we investigate here a general case, a periodic system with one atom per primitive cell, whose electron momentum density distribution leads to

$$n(\mathbf{p}) = \sum_{i\mathbf{k}} f_{i\mathbf{k}} \left|\int e^{-i\mathbf{p}\cdot\mathbf{r}} \psi_{i\mathbf{k}}(\mathbf{r}) d\mathbf{r}\right|^2. \qquad (1)$$

Here $\psi_{i\mathbf{k}}(\mathbf{r})$ is the electron wave function in the Bloch representation with i and $\mathbf{k}$ standing for its band index and crystal momentum, respectively, and $f_{i\mathbf{k}}$ is the occupation number. By using the local orbitals of the atom at $\mathbf{R}_I$, $\phi_i(\mathbf{r} - \mathbf{R}_I) = N^{-1/2}\Sigma_{\mathbf{k}} e^{-i\mathbf{k}\cdot\mathbf{R}_I} \psi_{i\mathbf{k}}(\mathbf{r})$, Eq. (1) can be reformulated in the Wannier representation as

$$n(\mathbf{p}) = \sum_i \frac{\Omega}{(2\pi)^3} \int f_{i\mathbf{k}} S(\mathbf{p}-\mathbf{k}) |\chi_i(\mathbf{p})|^2 d\mathbf{k}, \tag{2}$$

where $\chi_i(\mathbf{p}) = \int e^{-i\mathbf{p}\cdot\mathbf{r}} \phi_i(\mathbf{r}) d\mathbf{r}$is the Fourier transform of the local orbital and, according to the nearsightedness principle,[26] it is subject to a little change with the variation of the system size. In Eq. (2) $S(\mathbf{p}-\mathbf{k}) = N^{-1} |\Sigma_i e^{-i(\mathbf{p}-\mathbf{k})\mathbf{R}_I}|^2$represents the phase coherence of the local Wannier orbitals and it is just a δ function when the system is a perfect crystal of infinite size so that the orbitals at all $\mathbf{R}_I$ coherently contribute to $\mathbf{S}$ with a phase factor $e^{-i(\mathbf{p}-\mathbf{k})\mathbf{R}_I}$. However, if the dimension of the system is reduced to an embedded precipitate, only a few orbitals within the embedded precipitate contribute to $\mathbf{S}$ and thus $\mathbf{S}$ is no longer a δ function but a distribution function in momentum space, indicating that the electron momentum density of the embedded precipitate is that of the corresponding crystal convoluted with the smearing function $\mathbf{S}$. Fortunately, due to the positron confinement in ECNPs, the positron samples only those electrons in the ECNPs with phase coherence. Therefore, the observed momentum smearing is a quantum size effect of reducing the coherence length of the local orbitals.

Here, in order to estimate the localization radius of the Wannier orbitals, the maximally localized Wannier functions of bcc Cu is calculated by using the state-of-the-art scheme initiated by Marzari and co-workers.[27,28] As shown by our previous results,[29] in both bcc and fcc Cu, all the 3d electronic states are located at about 2 eV below the Fermi level and are fully occupied. Since the electronic states around the Fermi surface are s like, we focus on the s-state Wannier function. Figure 6 presents the real part of this s-state Wannier function of bcc Cu, calculated by using a $10 \times 10 \times 10$ regular k mesh in the first Brillouin zone (the imaginary part is vanishingly small). From the isodensities shown in Fig. 6, we can get a reasonable enough estimation for the localization radius of the Wannier function, i.e., $r = \sqrt{3}/2a = 0.249$ nm (with a the lattice constant of Fe, $a = 0.287$ nm). This localization radius is indeed comparable to the radii of the subnanoprecipitates. Although it is unnecessary for the Wannier orbitals around the precipitate boundaries to be the same as those of the bulk of bcc Cu, it is expected that the boundary Wannier orbitals do not significantly extend outside the ECNPs due to their spatially localized nature.

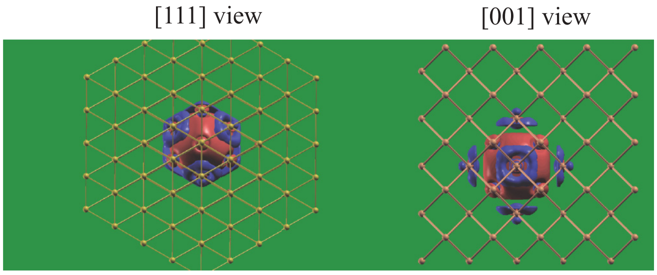

FIG. 6. (Color online) Real part of the s-state Wannier function of bcc Cu, calculated based on the maximally localized Wannier function scheme (Refs. 27 and 28). The absolute value of the isodensities is 0.5% of the maximum density and red and blue denote the positive and negative isodensities, respectively. The left side shows the [111] view and the right shows the [001] view.

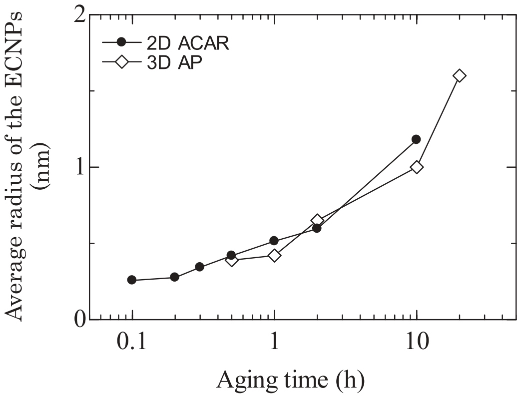

FIG. 7. Average radius of ECNPs estimated from the momentum smearing of 2D-ACAR distribution based on Eq. (3) (solid circles) and the average radius of ECNPs obtained by 3D-AP (open squares).

Approximating the summation over the position $\mathbf{R}_I$ in $\mathbf{S}$ by an integral over the volume of the precipitate, we get a universal smearing function as

$$S(q) \sim 9x^{-6}[-x\cos(x) + \sin(x)]^2,$$

where $x = r_0 q$ is a dimensionless variable with r_0 standing for the average radius of the precipitate. This is a Gaussian-like distribution function with a Gaussian FWHM of $2\pi/\sqrt{3}$. The appearance of the dimensionless variable in $\mathbf{S}$ has explicitly indicated an inverse dependence of the momentum smearing with the precipitate size. Taking the momentum distribution width Δp at the Gaussian FWHM of the smearing function, we get the scaling law

$$\Delta p = \frac{2\pi}{\sqrt{3}} r_0^{-1}. \tag{3}$$

Based on Eq. (3), the average radius of ECNPs is obtained using the Gaussian FWHM shown in Fig. 4(c) as Δp. The results are shown in Fig. 7 together with those obtained by a 3D-AP. It is noteworthy that the results agree with each other after every aging longer than 0.5 h, evidencing the validity of Eq. (3). In addition, as for (0.1–0.3)-h-aged samples, positron annihilation technique reveals the trend in the average radius of ECNPs of subnanometer in the very early stage of their formation, which is rather difficult to detect even by a 3D-AP. The exposed trend suggests that the radius gradually increases with aging time from 0.1 to 2 h.

Furthermore, it is shown that the effect of the broadening of the positron momentum distribution may become nontrivial with decreasing size of ECNPs. According to the theory of Saniz *et al.* based on the electron gas model,[25] the correction of the momentum smearing effect induced by the confined positron is about $\Delta p' \sim (1.13 - 0.93)/0.93\Delta p = 0.215\Delta p$, where Δp is the momentum smearing without the broadening effect of the positron momentum distribution. By using this result and the scaling law of Eq. (3), we can estimate the effect of the positron momentum broadening to the ECNPs radius r_0 as $\Delta r/r_0 \sim -\Delta p'/\Delta p = -0.215$, namely, about 22%. In particular, $\Delta p'$ is nontrivial only when the positron is very localized; for example, for $r_0 \sim 0.4$ nm in the 0.5-h-aged sample as the detection limit of the 3D-AP, the radius correction due to the positron momentum broadening effect can be estimated as $\Delta r \sim 0.215 \times 0.4 = 0.086$ nm, indicating that the effect of the broadening of the positron momentum distribution is indeed not significant.

It is demonstrated that positron annihilation technique quantitatively measures the average size of ECNPs larger than the size of the detection limit of the 3D-AP, about 0.4 nm, as shown in Fig. 7. It should also be noted that the present technique can detect the ECNPs with radii below 0.4 nm (for aging shorter than 0.5 h) and gives the same featured trend of the smearing reflecting the sizes of the ECNPs against aging time with that for longer aging as stated above. In contrast, the detection limits for "coherent" ECNPs in the Fe matrix are about 0.5 nm in radius by the other methods [high-resolution transmission electron microscope (HRTEM),[30] small-angle neutron scattering,[31] and 3D-AP (Refs. 32 and 33)]. It should be noted that even for the recent HRTEM it is very hard to observe the smaller coherent ECNPs because of the matrix Fe with ferromagnetic character and atomic number similar to that of the solute Cu. In consequence, it is demonstrated that the positron annihilation technique is a powerful tool used to obtain information on the size of the embedded Cu nanoprecipitates and subnanoprecipitates with positron affinitive trapping. Moreover, we emphasize that this method is also applicable to the other systems such as Al alloys, in which the complete confinement of positrons to the particles is possible, as we reported previously.[9]

V. CONCLUSION

The sizes of the embedded Cu nanoparticles in thermal-aged Fe-Cu alloys were estimated by using the unique characteristic of the positron affinitive confinement in the ECNPs. The smearing of the e^+-e^- momentum density distribution in the ECNPs after thermal aging was directly observed by 2D-ACAR measurements. The momentum smearing was found to be proportional to the inverse of ECNP radius, i.e., $\Delta p \propto r^{-1}$, where Δp is the momentum smearing width (FWHM) and r is the average radius of ECNPs. The proportional constant of the relationship was analytically obtained as $2\pi/\sqrt{3}$ and then the average radius was estimated and compared with those obtained by a 3D-AP. The results agree with each other for the ECNPs larger than 0.4 nm in radius, justifying the estimation method using positron confinement. It is noteworthy that the present technique can detect the ECNPs with their average radii above about 0.5 nm and furthermore gives the important trend in the average size below 0.5 nm as a function of aging time, which is rather difficult to detect even by a 3D-AP or other methods. Such identification and monitoring of the ECNPs in Fe matrix are important for understanding the embrittlement of reactor pressure vessel steels since the ECNPs play a significant role in the embrittlement.

ACKNOWLEDGMENTS

We thank B. Barbiellini for valuable discussion and our Information Science Group for use of the Hitachi SR8000 supercomputer. This work was partly supported by Radioactive Waste Management Funding and Research Center; by Grant-in-Aid for Scientific Research of the Ministry of Education, Culture, Sports, Science and Technology (Grants No. 15106015, No. 15360330, and No. 17002009); and by REIMEI Research Resources of Japan Atomic Energy Association. Z.T. was supported by the National Science Foundation of China (Grants No. 61076089 and No. 11175066) and the research programs of Shanghai (Program No. 09SG24) and of the Ministry of Education of China (New Century Excellent Talents in University and Scientific Research Foundation for Returned Overseas Chinese Scholars, State Education Ministry).

---

[1] K. Inoue, Y. Nagai, Z. Tang, T. Toyama, Y. Hosoda, A. Tsuto, and M. Hasegawa, Phys. Rev. B **83**, 115459 (2011).

[2] M. J. Puska, P. Lanki, and R. M. Nieminen, J. Phys.: Condens. Matter **1**, 6081 (1989).

[3] M. J. Puska, M. Šob, G. Brauer, and T. Korhonen, Phys. Rev. B **49**, 10947 (1994).

[4] W. J. Phythian and C. A. English, J. Nucl. Mater. **205**, 162 (1993).

[5] G. Brauer, M. J. Puska, M. Sob, and T. Korhonen, Nucl. Eng. Des. **158**, 149 (1995).

[6] W. J. Phythian, D. N. Diego, J. Mace, and R. J. McElroy, in *Effects of Radiation on Materials*, Proceedings of the 16th International Symposium ASTM STP 1175, edited by A. S. Kumar, D. S. Gelles, R. K. Nanstad, and E. A. Little (American Society for Testing and Materials, Philadelphia, 1994), pp. 462–491.

[7] Y. Nagai, M. Hasegawa, Z. Tang, A. Hempel, K. Yubuta, T. Shimamura, Y. Kawazoe, A. Kawai, and F. Kano, Phys. Rev. B **61**, 6574 (2000).

[8] Y. Nagai, T. Chiba, Z. Tang, T. Akahane, T. Kanai, M. Hasegawa, M. Takenaka, and E. Kuramoto, Phys. Rev. Lett. **87**, 176402 (2001).

[9] Y. Nagai, T. Toyama, Z. Tang, K. Inoue, T. Chiba, M. Hasegawa, S. Hirosawa, and T. Sato, Phys. Rev. B **79**, 201405 (2009).

[10] J. Laverock, S. B. Dugdale, M. A. Alam, M. V. Roussenova, J. R. Wensley, J. Kwiatkowska, and N. Shiotani, Phys. Rev. Lett. **105**, 236401 (2010).

[11] M. H. Weber, K. G. Lynn, B. Barbiellini, P. A. Sterne, and A. B. Denison, Phys. Rev. B **66**, 041305 (2002).

[12] A. Calloni, A. Dupasquier, R. Ferragut, P. Folegati, M. M. Iglesias, I. Makkonen, and M. J. Puska, Phys. Rev. B **72**, 054112 (2005).

[13] T. Chiba, Y. Nagai, Z. Tang, T. Akahane, M. Hasegawa, M. Takenaka, and E. Kuramoto, Mater. Sci. Forum **445-446**, 380 (2004).

[14] Z. Tang, T. Toyama, Y. Nagai, K. Inoue, Z. Q. Zhu, and M. Hasegawa, J. Phys.: Condens. Matter **20**, 445203 (2008).

[15] T. Toyama, Y. Nagai, Z. Tang, K. Inoue, T. Chiba, M. Hasegawa, T. Ohkubo, and K. Hono, TETSU TO HAGANE **95**, 118 (2009).

[16] M. Hasegawa, T. Chiba, A. Kawasuso, T. Akahane, M. Suezawa, S. Yamaguchi, and K. Sumino, Mater. Sci. Forum **196-201**, 1481 (1995).

[17] *Positron Spectroscopy of Solids*, edited by A. Dupasquier and A. P. Mills Jr. (IOS, Amsterdam, 1995).

[18] M. Hasegawa, Z. Tang, Y. Nagai, T. Chiba, E. Kuramoto, and M. Takenaka, Philos. Mag. **85**, 467 (2005).

[19] P. Asoka-Kumar, M. Alatalo, V. J. Ghosh, A. C. Kruseman, B. Nielsen, and K. G. Lynn, Phys. Rev. Lett. **77**, 2097 (1996).

[20] M. K. Miller, *Atom Probe Tomography* (Springer, New York, 2000).

[21] K. Hono, Prog. Mater. Sci. **47**, 621 (2002).

[22] Y. Nagai, Z. Tang, M. Hassegawa, T. Kanai, and M. Saneyasu, Phys. Rev. B **63**, 134110 (2001).

[23] Y. Nagai, T. Nonaka, M. Hasegawa, Y. Kobayashi, C. L. Wang, W. Zheng, and C. Zhang, Phys. Rev. B **60**, 11863 (1999).

[24] Z. Tang, M. Hasegawa, Y. Nagai, and M. Saito, Phys. Rev. B **65**, 195108 (2002).

[25] R. Saniz, B. Barbiellini, and A. Denison, Phys. Rev. B **65**, 245310 (2002).

[26] W. Kohn, Phys. Rev. Lett. **76**, 3168 (1996).

[27] N. Marzari and D. Vanderbilt, Phys. Rev. B **56**, 12847 (1997).

[28] I. Souza, N. Marzari, and D. Vanderbilt, Phys. Rev. B **65**, 035109 (2001).

[29] Z. Tang, M. Hasegawa, Y. Nagai, and M. Saito, Phys. Rev. B **65**, 195108 (2002).

[30] M. L. Jenkins and M. A. Kirk, *Characterization of Radiation Damage by Transmission Electron Microscopy* (Institute of Physics, Bristol, 2001).

[31] A. Ulbricht, F. Bergner, J. Bohmert, M. Valo, M. H. Mathon, and A. Heinemann, Philos. Mag. **87**, 1855 (2007).

[32] M. K. Miller and K. F. Russell, J. Nucl. Mater. **371**, 145 (2007).

[33] T. F. Kelly and M. K. Miller, Rev. Sci. Instrum. **78**, 031101 (2007).